ACS OMEGA

http://pubs.acs.org/journal/acsodf

Article

Iron Nanoparticles Wrapped with an N-Doped Carbon Material Produced by Using a Zinc Hydroxide Ferrocyanide Nanohybrid for Use in Commercial-like Supercapacitors

Mohammad Yeganeh Ghotbi,* Madineh Farhadi, and Fatemeh Abbasi

Cite This: *ACS Omega* 2023, 8, 22964−22974

Read Online

ACCESS | Metrics & More | Article Recommendations | Supporting Information

ABSTRACT: According to the technology of carbon-based supercapacitors, modifying the structure of carbon as an active electrode material leads to an increase in capacitance. A modification involves introducing heteroatoms such as nitrogen into the carbon structure and composing it with metals such as iron. In this research, an anionic source called ferrocyanide was used to produce N-doped carbon consisting of iron nanoparticles. In fact, ferrocyanide was located as a guest between the layers of a host material, which is zinc hydroxide in the α phase. This new nanohybrid material was then heat-treated under Ar, and the heated product after acid washing was iron nanoparticles wrapped with N-doped carbon materials. This material was used as an active material in the production of symmetric supercapacitors with different organic ($TEABF_4$ in acetonitrile) and aqueous (sodium sulfate) electrolytes as well as a new electrolyte (KCN in methanol). Accordingly, the supercapacitor made by the N/Fe-carbon active material and the organic electrolyte showed a capacitance value of 21 F/g at a current density of 0.1 A/g. This value is comparable to and even higher than the values observed in commercial supercapacitors.

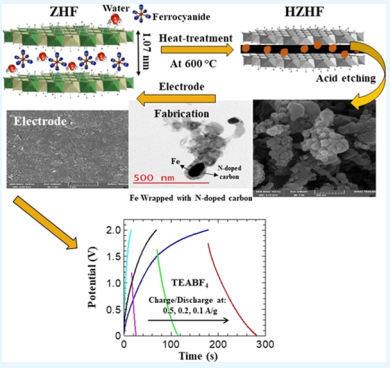

1. INTRODUCTION

To increase the energy storage capacity for supercapacitors (SCs) or electric double-layer capacitors (EDLCs), researchers have used two main routes. Since SCs with a simple physics benefit from the adsorption/desorption of electrolyte ions on the electrode surface, the first way is to increase the available surface area (ASA) of the electrode's material (usually carbon) to accommodate more electrolyte ions.[1] In addition, the second way is the introduction of some dopants such as nitrogen, sulfur, boron, *etc.*, in the carbon lattice.[2−4] This doping process is thought to lead to increased electron mobility, surface wettability improvement for aqueous electrolytes, reducing the diffusion resistance of electrolyte ions, and introducing pseudo-capacitive property for carbon materials, resulting in an improvement in the specific capacitance. On the other hand, nonprecious metal catalysts (NPMCs) have been used for many years in catalyzing the oxygen reduction reaction (ORR) of polymer electrolyte fuel cell (PEFC) cathodes.[5,6] One of the most important NPMCs is in the form of metal-N_x coordination, where the metal is often Ni, Co, or Fe.[5,6] Nitrogen in carbon lattice acts as an N-dopant and donates electrons to the carbon and the metal acts as an active electrocatalyst center for enhancing the ORR activity. Recently, Fe/N-doped carbon material has been used as an active material for use in SC electrodes.[7−9] It is claimed that the presence of iron would catalyze carbon graphitization during carbonization (a more efficient electron transport pathway) and boosts the double-layer capacitance.[8]

In our previous works, we used layered nanoreactors to synthesize highly porous metal/N-doped carbon materials to be used as efficient catalysts for the ORR and SC electrodes.[3,5] In this work, we use a layered nanohybrid called zinc hydroxide ferrocyanide as the precursor for the production of iron nanoparticles wrapped with N-doped carbon material as an active material in the production of symmetrical SC devices. We prepared SC electrodes in a commercial-like way and used different aqueous and organic electrolytes to investigate their performance.

2. MATERIALS AND METHODS

2.1. Material Synthesis. The materials used in this work were prepared as follows: First, a layered hydroxide material called zinc hydroxide nitrate (ZHN) was synthesized according to our previous works.[10] The zinc hydroxide ferrocyanide (ZHF) nanohybrid was prepared by contacting 1 g of the ZHN into a 200 mL solution of 0.2 M potassium ferrocyanide for 6 h. The ZHF was thoroughly washed in deionized water, ethanol, and acetone and then dried at 70 °C, overnight. After

Received: March 25, 2023
Accepted: June 5, 2023
Published: June 15, 2023

© 2023 The Authors. Published by American Chemical Society

https://doi.org/10.1021/acsomega.3c02017
ACS Omega 2023, 8, 22964−22974

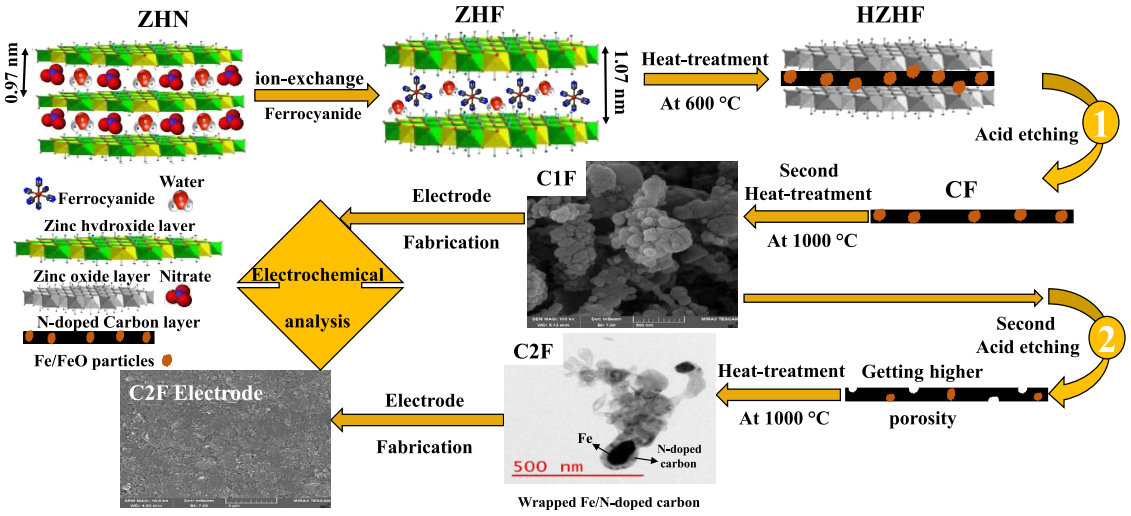

Figure 1. Schematic diagram of the synthesis of the carbon materials in this work.

that, ZHF was heat-treated at 600 °C in an electric tubular furnace under an argon atmosphere at a flow rate of 50 mL/min for 1 h at a rate of 10 °C/min and then cooled down naturally under an argon atmosphere. To obtain carbon material and remove the produced metal oxide during the heating, the heat-treated nanohybrid (HZHF) was added in 1 M HCl (1 g solid/200 mL) at room temperature for 12 h and was then washed in distilled deionized water, ethanol, and acetone and finally dried at 70 °C, overnight. The as-prepared carbon material (CF) was again heat-treated at 1000 °C under an argon atmosphere (flow rate of 50 mL/min for 1 h at a rate of 5 °C/min),[11] and this sample was named C1F. The C1F was again acid etched in 3 M H_2SO_4 (1 g solid/200 mL) at 50 °C for 5 days to remove any uncoated iron nanoparticles (with carbon layers) and was again heat-treated at 1000 °C under an argon atmosphere following washing and drying. This new sample was named C2F.

2.2. Physical Characterization. X-ray diffraction (XRD) patterns were collected on a Unisantis XMD300 powder diffractometer unit using Cu Kα (λ = 1.5418 Å). FTIR spectra were recorded using a Bruker α II spectrophotometer in the range of 400−2000 cm^{-1}. Thermal properties of the ZHF nanohybrid were determined using an SDT Q600 V20.9 Build 20 instrument operated under an argon atmosphere at a flow rate of 50 mL/min from 25 to 720 °C at a rate of 5 °C/min. The morphologies and texture of the carbon materials were characterized using a field emission scanning electron microscope (FESEM) (MIRA3, TESCAN) and a transmission electron microscope (FEI Tecnai F20 at 200 kV). Elemental analysis was also performed by using energy-dispersive X-ray spectroscopy (EDS, XFlash 6130 detector, Bruker). The surface area and pore size distribution of the carbon materials were determined using a BELSORP measuring instrument (BELSORP-mini, Japan, Inc.) using nitrogen gas adsorption−desorption technique at 77 K. X-ray photoelectron spectroscopic (XPS) measurement was performed on a Thermo Scientific K-Alpha X-ray photoelectron spectroscope using Al Kα and spot size 400 μm.

2.3. Electrochemical Tests. First, a paste was prepared by mixing PVDF, acetylene black, and each carbon sample in NMP (80 mg of carbon material, 10 mg of acetylene black, and 10 mg of PVDF binder) and the paste was then coated onto an aluminum foil (as the current collector) using a homemade doctor blade. After coating the paste on the foil surface, the electrode was dried on a heater plate at 85 °C. The dried electrode was pressed using a uniaxial press with a pressure of 100 MPa for 2 min. The electrode material thickness on the aluminum foil was ≈45 μm and mass loading of the active electrode material was ≈4 to 5 mg/cm^2. Two pieces of each electrode were assembled with a nonwoven hydrophilic polyolefin, as the separator, sandwiched in between for fabrication of supercapacitors. 1 M sodium sulfate in water, 0.6 M potassium cyanide in methanol, and 0.4 M tetraethyl ammonium tetrafluoroborate ($TEABF_4$) in acetonitrile have been used as various aqueous and organic electrolytes. Cyclic voltammetry (CV), galvanostatic charge−discharge cycles, and electrochemical impedance spectroscopy (EIS) analyses were performed using a potentiostat/galvanostat (Autolab PGSTAT204) instrument. The EIS measurements were carried out in the frequency range from 0.01 Hz to 100 kHz at the open circuit potential (V_{OCP}) with an AC amplitude of 10 mV. The capacitance value of the supercapacitors was calculated from their discharge curves according to the following equations[11,12]

$$C_{SC} = 4It/m\Delta V \quad (1)$$

where I is the discharge current, t is the discharge time, ΔV is the potential window, and m is the mass of the active material for both electrodes used in the fabrication of each supercapacitor. In addition, the energy density (E_{SC}, in Wh/kg) and power density (P_{SC}, in W/kg) of the symmetrical supercapacitors were determined using eqs 2 and 3[11] by using the galvanostatic charge−discharge curves measured at different current densities of 0.1−1 A/g.

$$E_{SC} = C_{SC}\,\Delta V^2/2 \times 3.6 \quad (2)$$

$$P_{SC} = E_{SC} \times 3600/t_{discharge} \quad (3)$$

3. RESULTS AND DISCUSSION

3.1. Physical Characterization of the Layered and Carbon Materials. Figure 1 shows the schematic diagram for the carbon synthesis and electrode making in this research. First, ZHN was synthesized and its nitrate anions were completely replaced by ferrocyanide by a simple ion-exchange process to produce ZHF. XRD patterns for the ZHN

https://doi.org/10.1021/acsomega.3c02017
ACS Omega 2023, 8, 22964−22974

precursor, the ZHF nanohybrid, and HZHF are shown in Figure S1. As shown in the figure, both precursor and nanohybrid have α-phase brucite-like structures with different basal spacing peaks around 0.97 and 1.07 nm for the ZHN and ZHF, respectively.[2] The lack of the peak around 0.97 nm for ZHF reveals the complete ion-exchange process of bigger-size ferrocyanide for nitrate anions between zinc hydroxide layers in the ZHN precursor.

The XRD pattern for HZHF is also shown in Figure S1. This pattern clearly shows the characteristic peaks for zinc oxide (zinc hydroxide to oxide during heating) in the zincite phase (card no. 36-1451) accompanied by new phases. These new phases are attributed to zinc ferrocyanide with card no. 01-0433, graphitic carbon with a peak around 26.5° (card no. 41-1487), and there is a small peak around 61° that is due to iron oxide with card no. 06-0711. The HZHF was subjected to mild acid conditions to remove oxide phases such as zinc and iron oxide and to produce more porosity (CF sample). The XRD pattern of CF shows the residual phases of HZHF after acid etching. This pattern shows zinc ferrocyanide (ZFC) and graphitic carbon peaks. The CF sample was again heat-treated at 1000 °C under an Ar atmosphere to remove ZFC and obtain graphitic carbon with higher crystallinity and conductivity (C1F).[11] The XRD pattern of the C1F sample shows two phases including graphitic carbon and metallic cubic iron with a peak around 44.7° (card no. 06-0696). According to the above results, ZFC was produced during heat treatment of the ZHF nanohybrid. In addition, ZFC is stable up to 600 °C and is stable in mild acidic conditions and is insoluble. ZFC decomposes at 1000 °C and Zn vaporizes on the carbon surface above 750 °C.[5] The cyanide ions are converted to graphitic carbon, that is, cyanide acts as a precursor of soft carbon under heat treatment. Because of the presence of an iron peak in the XRD pattern of C1F (and the presence of an iron peak in the electrochemical tests), some iron nanoparticles appear to exist in an uncoated form (with carbon layers) and should be removed by additional acid washing. Accordingly, the second acid wash was performed on the C1F sample and it was again subjected to heat treatment at 1000 °C. Figure S1 also shows the XRD pattern of this new sample (C2F). As can be seen, C2F shows only the characteristic peaks of graphitic carbon and the iron content in this sample is so low that it cannot be detected by XRD (confirmed by EDX analysis).

Figure S2a shows FTIR spectra for the ZHN, potassium ferrocyanide (KFC), ZHF, and its heat-treated product (HZHF). In addition, FTIR spectra for all carbon-derived layered nanohybrid materials are shown in Figure S2b. In the FTIR spectrum of the ZHN, metal oxide/hydroxide peaks at low wavenumbers of 436 and 470 cm^{-1} are seen and the nitrate anion characteristic peaks are around 840 and 1380 cm^{-1} (bending and stretching, respectively).[13] FTIR spectrum for potassium ferrocyanide shows a peak at around 640 cm^{-1} due to the Fe−CN bond and a sharp peak around 2030 cm^{-1} due to the cyanide group.[14,15] In the FTIR spectrum of the ZHF, the broad peak around 500 cm^{-1} is related to the metal oxide/hydroxide bond, the peak around 605 cm^{-1} is attributed to the Fe−C bond, and a bimodal peak around 2070 and 2120 cm^{-1} is due to Fe−CN−Zn. This bimodal peak is due to the fact that in the ion-exchange process, some iron element in the ferrocyanide group is converted from II to III oxidation state.[16] The peak at 2070 cm^{-1} is due to the II state and the peak at 2120 cm^{-1} is attributed to the III oxidation state.[16,17] The absence of the peak around 2030 cm^{-1} is attributed to the absence of free cyanide groups in the ZHF nanohybrid.[18] In fact, when the ferrocyanide group is coordinated with the transition metals, the charge density in nitrogen moves toward the transition metal; as a result, the C≡N bond energy changes to higher values, resulting in higher wavenumbers observed in the FTIR spectrum.[19] The HZHF sample shows a huge FTIR peak around 506 cm^{-1} due to a large amount of zinc oxide phase.[13] In addition, there are some other peaks such as the peak at 2042 cm^{-1} due to the free cyanide group of ZFC.[18] These results are consistent with the data of XRD analysis.

Figure S2b represents the FTIR spectra of the carbon materials. For the CF sample, the spectrum includes three peaks around 494, 599, and 2095 cm^{-1}, which are attributed to Zn−N, Fe−C, and free cyanide groups from ZFC contribution in the sample.[15,16] The absence of a large and broad peak at around 500 cm^{-1} indicates the removal of the ZnO phase from HZHF after the mild acid etching process. For both C1F and C2F samples, the FTIR spectra show two weak and broad peaks around 1295 and 1580 cm^{-1}, which are related to C═N/C−C and C═C/C═O stretching vibrations, respectively.[3,5] As can be seen, the peaks due to ZFC have been completely removed by heating the sample at 1000 °C. In addition, the absence of the peaks around 600−400 cm^{-1} indicates that despite the presence of iron in the samples, iron is in the metallic form, but not in the oxide form.

Figure S3 shows the TG/DTG curves for the ZHF. ZHF decomposes in two major steps and some minor steps. The first major step is attributed to the removal of the intercalated/adsorbed water molecules with a respective weight loss of 6.7% at a maximum temperature of 117 °C.[13] The second important step is due to the collapse of the layered material and the transformation of the hydroxide into the oxide phase along with the thermal decomposition of the ferrocyanide group into N-doped carbon materials. This thermal collapsing and decomposition continues up to 600 °C with 12.5% weight loss. That is, the remaining weight up to the temperature of 600 °C is about 80%. The equations of the above steps are as follows

$$2Zn_5(OH)_8(NO_3)_2\cdot nH_2O \rightarrow Zn_{10}(OH)_{16}(Fe(CN)_6)\cdot nH_2O,\ \text{ion} - \text{exchange} \quad (4)$$

$$Zn_{10}(OH)_{16}(Fe(CN)_6)\cdot nH_2O \rightarrow Zn_{10}(OH)_{16}(Fe(CN)_6),\ \text{first step} \quad (5)$$

$$Zn_{10}(OH)_{16}(Fe(CN)_6) \rightarrow 10ZnO + 6H_2O + Fe + C_XH_Y + N_2 + NO_X + CO_X + N - \text{doped carbon},\ \text{second step} \quad (6)$$

Since it was observed that zinc oxide is easily reduced and volatilized on the carbon surface (especially in the presence of iron)[5] and as seen in Figure S3, at temperatures above 600 °C, the weight loss rate decreases, therefore, thermal analysis was performed up to 720 °C. Our experimental results also show that heat treatment of ZHF at 600 °C gives more carbon materials than other temperatures of 650, 700, and 750 °C.

The adsorption−desorption isotherms for the C1F and C2F carbon materials are shown in Figure S4. The isotherms are of IVa type with H3 type hysteresis loop according to the IUPAC

https://doi.org/10.1021/acsomega.3c02017
ACS Omega 2023, 8, 22964−22974

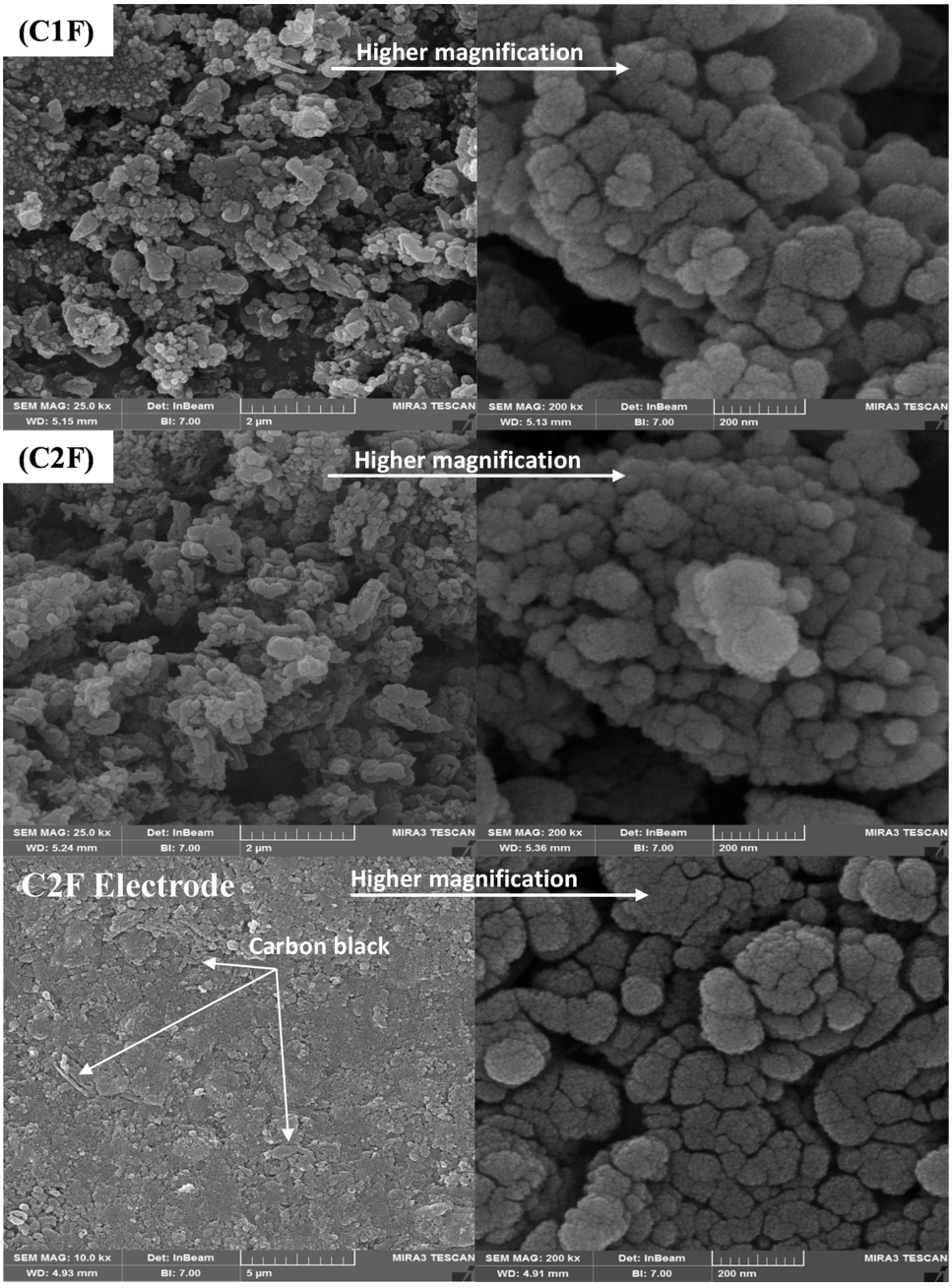

Figure 2. FESEM images of the C1F, C2F, and the surface of an electrode prepared by using the C2F carbon material (white arrows show Super P carbon black particles).

nomenclature.[20,21] Plate-like carbon materials containing slit pores show this type of isotherm and hysteresis loop.[21] According to the IUPAC nomenclature, aggregates with platelet particles show the H3 hysteresis loop without any limiting adsorption at high p/p^0. This is due to the presence of macropores in the samples (see the circle at high p/p^0 in Figure S4). In addition, nitrogen adsorption at very low p/p^0 for sample C1F indicates the absence of micropores in a significant amount for this sample (see the circle at low p/p^0 in Figure S4). These data are confirmed by Barrett–Joyner–Halenda (BJH) and Micro Pore (MP)-plot analyses.

The BJH pore size distributions of the C1F and C2F carbon materials are observed in Figure S5. The BJH pore size distribution for both samples shows bimodal distributions of about 2.4 and 35 nm with a small amount of macroporosity. Moreover, the pore size distribution of the samples obtained by the MP method shows a monomodal distribution of around 2 nm. Accordingly, BJH and *MP* pore size distributions confirm that most of the pore volume is in the mesoporous range centered around 2 nm for both carbon materials. The Brunauer–Emmett–Teller (BET), BJH, and MP-plot analysis data for the carbon materials are given in Table S1. In general, the surface area values for both samples are not high. This is due to the graphitic structure of carbon materials and the presence of iron (with a much higher molar mass compared to carbon) in the carbon structure. As one can see in Table S1, after the second acid washing for the C1F, the new sample (C2F) shows up to a 55% increase in the surface area value as well as about a 12% increase in the mean pore volume. Although the pore volume for C2F is still not significant, it is 3

https://doi.org/10.1021/acsomega.3c02017
ACS Omega 2023, 8, 22964−22974

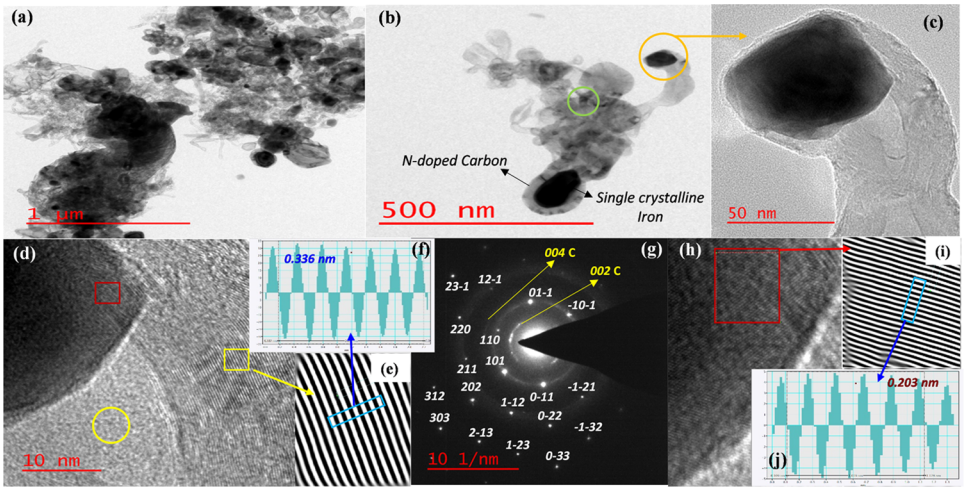

Figure 3. HRTEM images of the C2F sample, iron, and carbon crystalline structures. (a) Image at low magnification; (b) a distinct particle; and (c–j) the structure and texture of the carbon coating an iron particle.

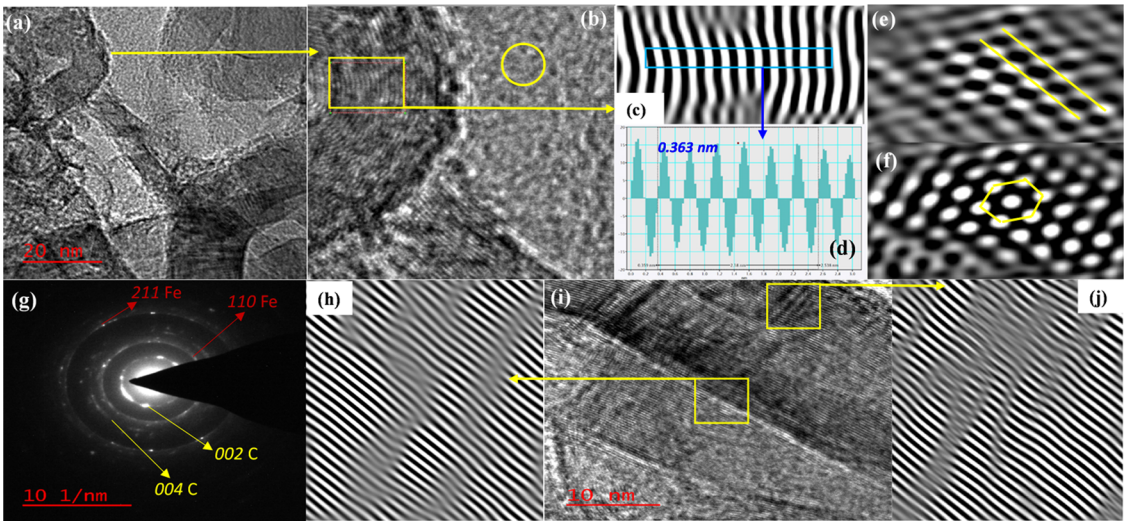

Figure 4. HRTEM images of the C2F sample and crystalline defects of the carbon material. (a–d) Bent region of the carbon crystal layers; (e, f) edge and top views of crystalline graphitic carbon; (g) SAED pattern for the low-magnification image of Figure 3a; and (h–j) twisted regions in the carbon structure.

times larger than that of C1F. These micropores were created by the second acid wash and removal of unprotected iron nanoparticles. The data obtained by BET, BJH, and MP-plot analyses are in perfect agreement with the data observed by adsorption–desorption isotherms. It has been found that the existence of micropores in the active materials of EDLC electrodes is very important for increasing the capacitance due to the effect of pore confinement for electrolyte ions. So, electrolyte ions, especially monovalent ions, can insert themselves inside the micropores (as desolvated or partially solvated form) to increase the capacitance.[22]

SEM micrographs of C1F, C2F, and the electrode surface prepared by using C2F carbon material at different magnifications are shown in Figure 2. SEM images of C1F and C2F powders show small and larger particles with a velvety and porous structure. These pores are caused by the release of carbon and nitrogen oxides as well as water vapor during carbon synthesis, and the removal of zinc oxide and iron particles in the acid washing process. In addition, the morphologies of C1F and C2F do not show a significant difference. The electrode surface prepared using the C2F sample is also shown in Figure 2. As can be seen, the smooth and seamless surface is observed at low magnification and at higher magnification, there are small slits, which are suitable channels for the penetration of electrolyte ions. Pressing at 100 MPa did not change the size and shape of the particles, as the particles appeared to be powder-like. White arrows in the figure show Super P carbon black particles on the electrode surface.

HRTEM analysis was performed to investigate the texture, porosity, amorphous or crystalline nature, and the presence of iron particles in the C2F carbon structure. Figures 3 and 4 show the HRTEM images for the C2F. We started with a low-magnification image (Figure 3a) to show the texture of the particles. Figure 3b shows a distinct particle. This particle has carbon and iron regions. Figure 3c–j shows the structure and texture of the carbon-coated iron particle. Crystal regions were reproduced by Gatan software (GMS 3), and an interlayer *d*-spacing of 0.334 nm was observed for the crystalline carbon region of sample C2F, as shown in Figure 3f. This *d*-spacing is

https://doi.org/10.1021/acsomega.3c02017
ACS Omega 2023, 8, 22964–22974

consistent with 002 pure graphite. Figure 3g shows the SAED pattern of a carbon-coated iron particle (orange circle in Figure 3b). The SAED pattern shows graphite layers in addition to single-crystal iron dots. Figure 3h–j shows the crystalline layers of the iron particle with a *d*-spacing of 0.203 nm perfectly consistent with the 100 plane of α phase cubic iron (card no. 06-0696). The SAED pattern for the iron single crystal was indexed using CrysTbox software.[23]

Figure 4a–d shows the bent region of the carbon crystal layers (green circle in Figure 3b). As seen, *d*-spacing is larger in curved regions (0.363 nm versus 0.336 nm for pure graphite). The yellow circles in Figures 3 and 4 show amorphous regions. Figure 4e,f shows edge and top views of crystalline graphitic carbon. Figure 4g shows a SAED pattern for the low-magnification image of Figure 3a, which contains several particles. As shown, in this situation, SAED shows polycrystalline structures for iron and carbon materials. Figure 4h–j shows that in addition to the bent regions in the graphite carbon layers, there are also twisted regions in the carbon structure. In general, using the results observed by XRD, HRTEM, and SAED analyses, the C2F material contains amorphous and crystalline carbon regions as well as single-crystal cubic iron particles coated with carbon layers.

The EDS analysis results for the C1F and C2F samples are given in Figure S6. In addition, the elemental percentages of the samples are presented in Table S2. As shown, the second acid wash results in a drastic reduction of the iron percentage for C1F to C2F (with about 7% weight loss). However, this long and highly acidic condition results in an increased oxygen content (about 4%) for C2F compared to its parent, C1F. The C2F contains about 11.7% (wt/wt) oxygen, 6.3% nitrogen, and 2% iron.

Figure S7a shows the XPS survey scan of the C2F. The XPS spectrum of the material contains four photoelectron peaks of carbon, nitrogen, oxygen, and iron at peak binding energies of around 284.5 eV (C 1s), 399.5 eV (N 1s), 532 eV (O 1s), and 707 eV (Fe 2p). The C2F has atomic concentrations of 83.81% carbon, 9.87% oxygen, 5.81% nitrogen, and 0.51% iron, which are in good agreement with the data observed by the EDS analysis. Further analyses were performed on the C 1s and the N 1s signals, as shown in Figure S7b,c. The fitting of the C 1s spectrum was resolved into five peaks at 284.5 eV (59.9%), 285.8 eV (13.8%), 287.1 eV (6.4%), 288.5 eV (5.6%), and 290.6 eV (14.3%).[6,9] The C–N bond has a binding energy of about 286 eV, and graphitic carbon with a well-ordered structure and sp^2 hybridization has a binding energy of 284.5 eV.[24,25] The C–O/O–C–O/–C=O functional group signals can be found between 287 and 291 eV, that is, between the satellite structure for graphitic carbon and the C–C peak. This is due to the oxidation of several graphene layers with an oxygen content of about 10%.[24] The fitting of the N 1s spectrum was resolved into two peaks at 400.1 eV (90%) and 398.2 eV (10%). The peak with less binding energy is due to pyridinic (N-6) nitrogen, where one N atom with two C atoms are hybridized as sp^2 hybridization and it is located on the edge of the graphite plane. The peak with higher energy is attributed to pyrrolic nitrogen (N-5) with the same hybridization, but another configuration, where N is bonded to two carbons and one hydrogen in a pentagonal heterocyclic ring of C atoms.[24,25] According to the results obtained by HRTEM and XPS analysis, it can be concluded that the insertion of nitrogen in the carbon structure was done in the amorphous region of the carbon sample and not in the graphitic carbon region. Note that the pseudo-capacitance behavior of N-doped carbon materials strongly depends on the content of pyrrolic nitrogen, that is, pyrrolic nitrogen is a very active capacitive site and is an efficient case for improving the electrochemical performance in EDLCs.[24]

3.2. Electrochemical Analyses of the SCs. Full-cell symmetrical SCs were made according to Section 2.2 to investigate the behavior of the C1F and C2F carbon materials when used as real SC electrodes. In this work, organic ($ETABF_4$ in acetonitrile) and aqueous electrolytes (sodium sulfate in water) were used in the SCs for comparison. Moreover, a new electrolyte, i.e., KCN salt in methanol has been used in this work due to its small ions and the presence of ultramicropores (pore width <0.7 nm)[20] in our carbon materials (see surface area analysis). It is known that the ion size (as desolvated or partially solvated) of the electrolyte must be approximately equal to the pore size of the electrode material to contribute to the capacitance.[26]

Figure 5 shows the CV plots of the C1F SCs assembled using sodium sulfate ($C1F_S$) and KCN ($C1F_K$) electrolytes

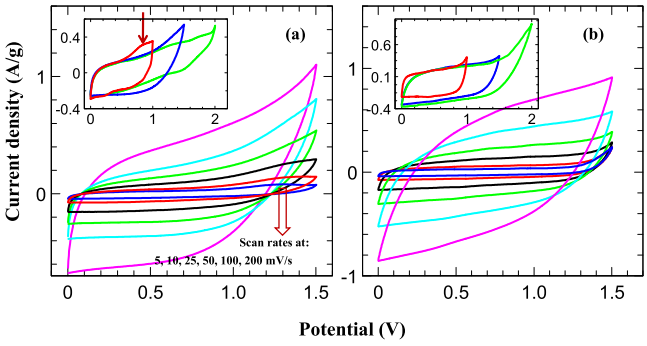

Figure 5. CV curves of the C1F SC with (a) sodium sulfate electrolyte and (b) KCN electrolyte.

with sweep rates of 5–200 mV/s in a potential window of 1.5 V. Moreover, the inset in the figures shows the CV plots of the C1F SCs with a sweep rate of 50 mV/s in different potential windows. As observed in Figure 5, the existence of a pair of broad Red-Ox peaks around 0.7 V (shown by brown arrows in the figure) is due to the presence of the uncoated iron nanoparticles on the C1F carbon surface.[27] The presence of these Red-Ox peaks made us use the second acid wash to remove uncoated iron particles to produce C2F samples. As can be seen in the figure, the SC with both electrolytes shows a rectangular shape, especially at low sweep rates. The rectangular shape of the CV for the $C1F_K$ SC is more perfect due to the better balance in polarization in the left (negative) and right (positive) regions of the CV curve. This is due to the almost equal size of the cation and anion of the electrolyte. At higher sweep rates, a deviation from the rectangular shape is observed, which is due to the limitation of ion incorporation into the electrode material.[11] Nevertheless, an increase in current density is observed at higher scan rates, as is the case in an ideal electric double-layer capacitor.[11]

Figure 6 shows the CV plots of the C2F SCs assembled using the mentioned electrolytes in addition to the well-known commercial electrolyte, namely $ETBF_4$ in acetonitrile in different sweep rates and potential windows. As shown in the figures, the Red-Ox iron peaks in the CV curves disappeared due to the removal of uncoated iron nanoparticles during the second acid wash. More rectangular shapes are seen

https://doi.org/10.1021/acsomega.3c02017
ACS Omega 2023, 8, 22964–22974

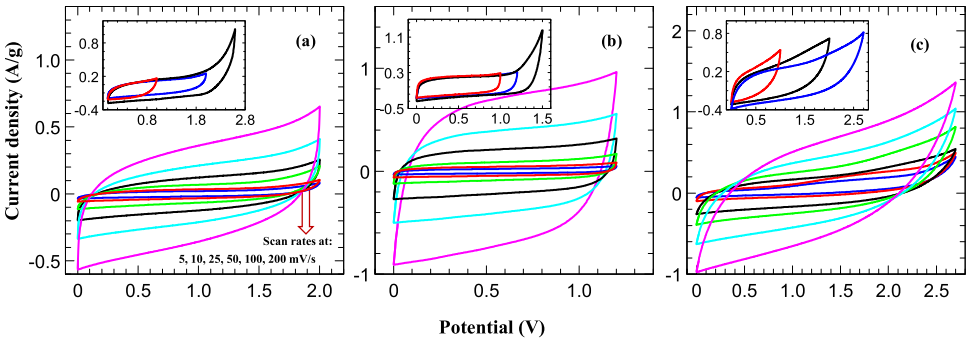

Figure 6. CV curves of the C2F SC with (a) sodium sulfate electrolyte, (b) KCN electrolyte, and (c) $TEABF_4$ electrolyte.

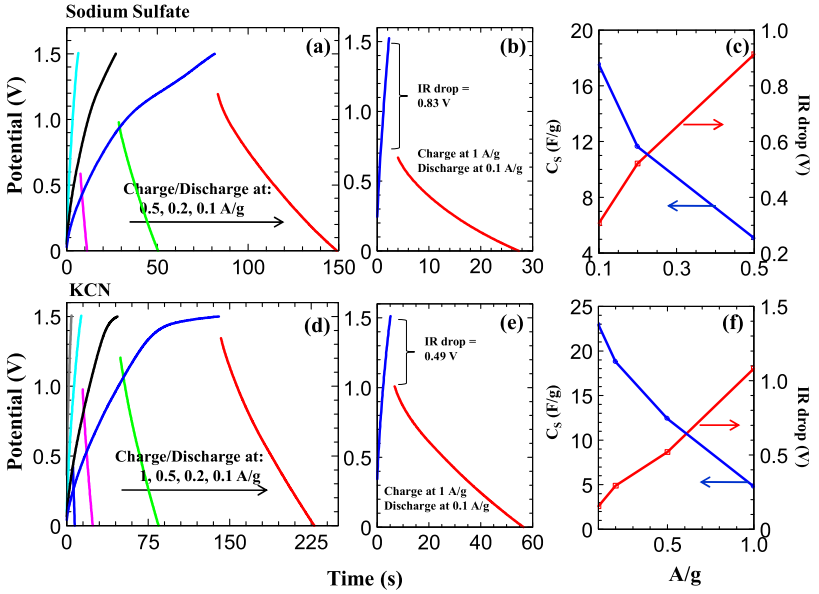

Figure 7. Galvanostatic charge−discharge curves of the C1F SC with (a−c) sodium sulfate electrolyte and (d−f) KCN electrolyte.

for the KCN electrolyte, probably due to its smaller ion size. Furthermore, as expected, a wider potential window is observed for the SC with organic electrolytes.

Typical charge−discharge (CDG) curves of the $C1F_S$ and $C1F_K$ SCs at different current densities with a potential window of 1.5 V are shown in Figure 7. In addition, the CDG analysis data for all SCs are given in Table S2. The C_s value for the $C1F_S$ SC is 17.5 F/g at a current density of 0.1 A/g in the 1.5 V potential window. The IR drop value in this process is significant (0.31 V). Figure 7b shows a fast charge (1 A/g)−slow discharge (0.1 A/g) for the $C1F_S$ SC with a C_s value of 5.9 F/g, i.e., it is a 34% typical slow charge and discharge. Moreover, the IR drop in this case is very high (0.83 V). As the current density increases from 0.1 to 0.5 A/g, the C_s values decrease and IR drop values increase in an almost linear relationship (see Figure 7c). The reason is the lack of enough time for the complete absorption/discharge process of electrolyte ions in the pores of the active material. Figure 7d−f shows CDG curves of the $C1F_K$ SC at different current densities with a potential window of 1.5 V. This SC shows an IR drop of 0.15 V and a C_s value of 22.9 F/g at a current density of 0.1 A/g, which is about 31% higher capacitance than $C1F_S$ SC. A fast charge (1 A/g)−slow discharge (0.1 A/g) for this SC shows a C_s value of 13.3 F/g with an IR drop of 0.44 V. Accordingly, by comparing the CDG curves for both SCs made by the same electrode materials and different electrolytes, it can be seen that the SC made using KCN electrolyte ($C1F_K$) shows higher performance than the SC with sodium sulfate electrolyte ($C1F_S$).

CDG curves of the SCs assembled with C2F active material and various electrolytes of sodium sulfate ($C2F_S$), KCN ($C2F_K$), and $TEABF_4$ ($C2F_T$) electrolytes at different current densities and potential windows are shown in Figure 8 (the CDG analysis data are also presented in Table S3). For the $C2F_S$ SC, the C_s value is 13.7 F/g at a current density of 0.1 A/g. This value is less than that for the $C1F_S$ SC with the same electrolyte. However, $C2F_S$ exhibits a lower IR drop value than $C1F_S$ SC at the same current density, and the potential window for $C2F_S$ SC is wider (2 V) than $C1F_S$ (1.5 V), resulting in a higher power density for $C2F_S$ than $C1F_S$. As for $C2F_K$ SC, first, we used the same potential window as $C1F_K$ SC for better comparison. However, as we also saw for $C1F_K$ SC, in the potential window of 1.5 V, the Coulombic efficiency is low (Figure 7d, also see Figure 8d) and we used a lower potential window (1.2 V) for $C2F_K$ SC. The capacitance is 19.2 F/g for $C2F_K$ SC at a current density of 0.1 A/g, much higher than that of $C2F_S$ SC (40%). In addition, in this case, the IR drop value is as low as 0.08 V. Additional data for $C2F_K$ SC are given in Table S3. Finally, as previously mentioned, C2F SC was fabricated using a well-known commercial electrolyte, $TEABF_4$ in acetonitrile ($C2F_T$). The $C2F_T$ SC shows a C_s value of 20.6 F/g at a current density of 0.1 A/g with an IR

https://doi.org/10.1021/acsomega.3c02017
ACS Omega 2023, 8, 22964−22974

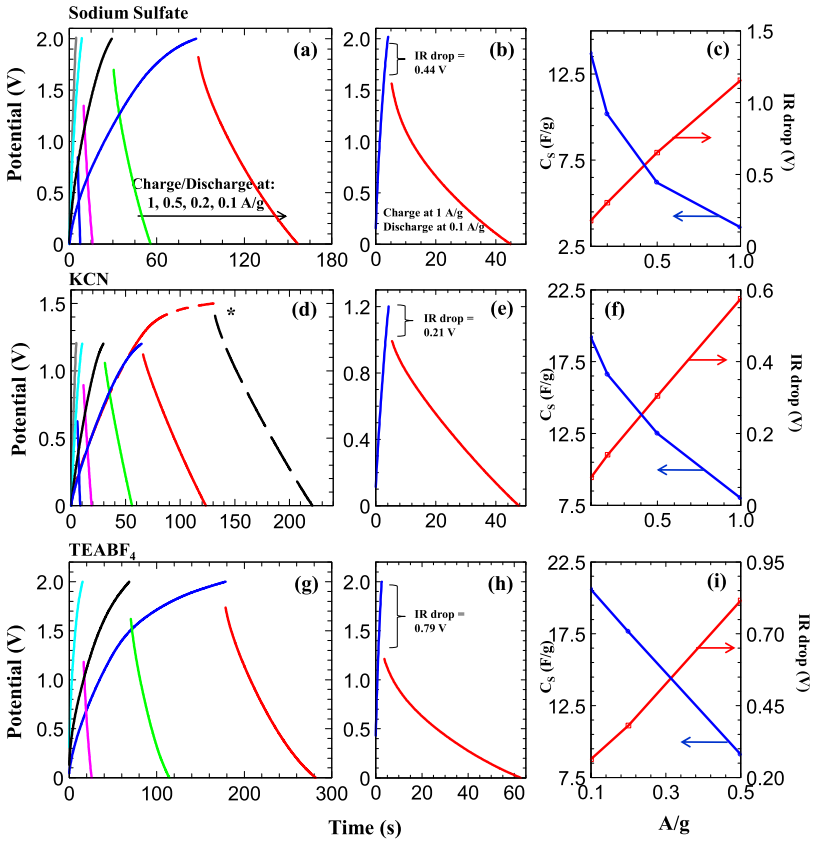

Figure 8. Galvanostatic charge−discharge curves of the C2F SC with (a−c) sodium sulfate electrolyte, (d−f) KCN electrolyte, and (g−i) $TEABF_4$ electrolyte.

drop value of 0.26 V in a potential window of 2 V. In fact, $C2F_T$ shows about 50% higher capacitance compared to $C2F_S$ with the same potential window.

Because of IR drop, in general, the amount of IR drop depends on electrode conductivity, electrolyte conductivity, and potential window applied to SC. So, the higher conductivity in the electrode and electrolyte as well as the lower potential window reduces the IR drop value.[28,29] Since in each series SC made by C1F and C2F, the electrodes have the same conductivity, the difference in voltage drop between SCs in each series is due to the applied potential window and electrolyte conductivity. Accordingly, SCs fabricated by organic electrolytes with lower conductivity show higher IR drop values than SCs fabricated by an aqueous sodium sulfate electrolyte with higher conductivity.[28]

Nyquist plots for C1F and C2F SCs obtained by the EIS study are shown in Figure 9. The enlarged view of the higher frequency part of the Nyquist diagram is also shown in the figure. The EIS analysis data for all SC devices are presented in Table S3. For each SC, there is a knee point in higher frequencies. The "knee" point resistance (R_{knee}) is the sum of equivalent series resistance (R_{ESR}) and ionic resistance (R_{ion}) values ($R_{knee} = R_{ESR} + R_{ion}$).[2,29] R_{ion} is the ionic resistance of the electrolyte ions inside the pores of porous materials.[29] The R_{ESR} is due to the sum of the resistance of the active material (and electronic resistance between the carbon particles), the bulk electrolyte resistance, and contact resistance between the active material and the current collector.[29,30] The amount of R_{ion} is controlled by the pore size, pore size distribution, and ion size of the electrolyte; so, if the size of the electrolyte ion is smaller than the pores, the ion mobility inside the pores is

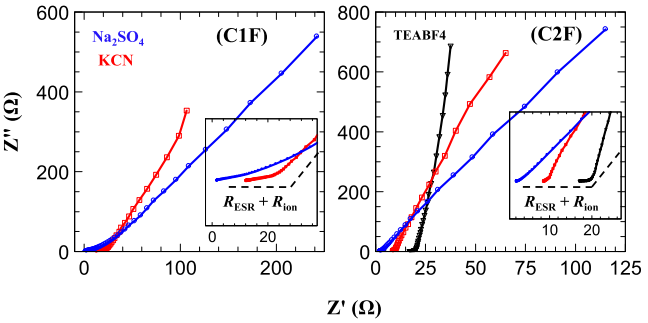

Figure 9. Nyquist plots for the C1F and C2F SCs with different electrolytes.

more and the R_{ion} is less.[29] It is well known that bulk electrolyte resistivity is lower for aqueous compared to organic electrolytes. Accordingly, as shown in Table S3, the minimum R_{ESR} in the case of sodium sulfate electrolyte was observed to be 1.6 and 2.2 Ω for active materials C1F and C2F, respectively. The slight difference between the two may be due to the higher amount of conductive metallic iron in the C1F sample. For both SCs made using KCN electrolyte, the R_{ESR} values are high, for example, the R_{ESR} value for $C1F_K$ SC is 12.2 Ω. In addition, the R_{ESR} value for the $C2F_T$ SC is as high as 16.9 Ω. Since for all C1F (or C2F) SCs, the electrodes are the same, the difference between the R_{ESR} values is due to the bulk electrolyte resistance values for the different electrolytes. Regarding the R_{ion} value, it should be noted that the mean pore volume for C2F powder is higher and the mean pore diameter is lower than C1F. That is, by using the second

https://doi.org/10.1021/acsomega.3c02017
ACS Omega 2023, 8, 22964−22974

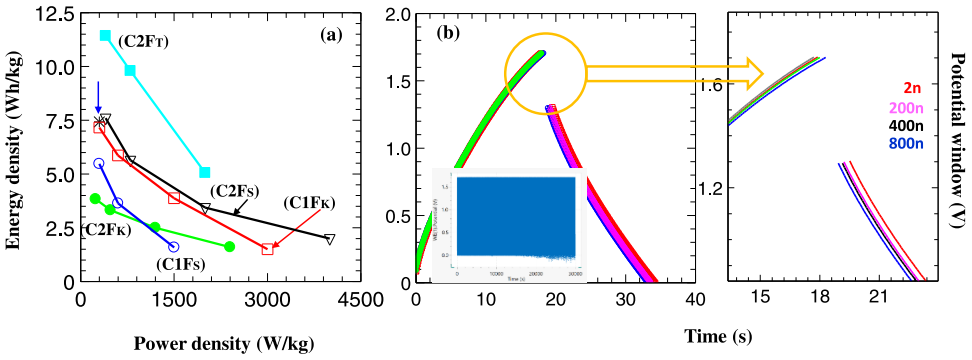

Figure 10. (a) Ragone plot of the symmetrical SC devices with different electrolytes obtained from their GCD curves (* in the figure represents the results for $C2F_K$ in 1.5 V potential window) and (b) capacitance retention of the $C2F_T$ SC measured at 2 A/g charge−discharge current density.

acid wash, the unprotected nano-iron particles are removed and new nanopores (in the micro region) are observed. Considering the mean pore size and volume of the C1F sample, a large R_{ion} value can be observed for the $C1F_S$ SC (13.4 Ω). If we consider the CV curve of $C1F_S$ SC, we can see that the left edge of the CV (negative polarization of the electrode) has a higher surface area than the right edge of the CV (positive polarization of the electrode). This means that when the electrode polarization is negative and sodium ions are adsorbed, the ability of the C1F material to adsorb electrolyte ions is greater than when the polarization is positive and large sulfate ions must be adsorbed.[26] Consequently, a large amount of R_{ion} value for the $C1F_S$ SC is probably due to less mobility of sulfate ions inside C1F pores. The R_{ion} value for $C2F_S$ SC (same electrolyte) decreased drastically due to the higher average pore volume for C2F, and its CV curve is quite symmetrical (see Figure 6a). In the case of the KCN electrolyte, the R_{ion} values for both $C1F_K$ and $C2F_K$ SCs are almost identical due to the smaller size of the cyanide ion than the sulfate ion, resulting in symmetrical CV curves for both $C1F_K$ and $C2F_K$ SCs. Finally, the R_{ion} value for the $C2F_T$ SC ($ETABF_4$ electrolyte) is as low as 2.8 Ω. This is attributed to the much larger size of $ETABF_4$ ions compared to KCN and sodium sulfate. So, the size of the $ETABF_4$ anion and cation is 0.48 and 0.68 nm, respectively (in the desolvated form).[26] Accordingly, the ions of this electrolyte basically do not enter into the ultramicropores and are adsorbed on the surface of the larger micropores. The Warburg resistance (in the low-frequency region) is attributed to the diffusion resistance of electrolyte ions to the electrode/electrolyte interface, the shorter the lines, the shorter the ion transport path and the lower the ion transport resistance.[11,30] For the SCs made using the C1F active material, the Warburg line for the KCN electrolyte is shorter than that for the sodium sulfate electrolyte due to the smaller size of the cyanide ion than the sulfate ion as mentioned earlier. This is the same for SCs made using C2F active material. However, in the case of $C2F_T$ SC ($ETABF_4$ electrolyte) with the much larger size of the electrolyte ions and the lack of access to the smaller pores of the carbon material, the adsorption/desorption process is easier and faster, resulting in a more vertical Warburg line for this SC compared to other SCs. This shows higher capacitance, lower diffusion resistance, and a purer double-layer capacitor behavior for the $C2F_T$.[11]

Figure 10a shows the Ragone plots of all SC devices. Although SCs show almost the same power density values, they show completely different energy density values. The maximum energy density value is observed for the $C2F_T$ SC, as this SC has an energy density of 11.43 Wh/kg at a power density of 400 W/kg. It is also observed that KCN electrolyte shows better performance than sodium sulfate for SCs fabricated using C1F and C2F active materials. The most important point is the fact that C2F with a lower iron content and higher porosity than C1F always shows a higher energy density value under the same conditions (the same electrolyte). The $C2F_T$ SC, at a higher power density of 2000 W/kg, still holds an energy density of 5.1 Wh/kg, which is comparable with commercial supercapacitors.[31,32]

A long-term galvanostatic CDG measurement was performed at a charge−discharge current density of 2 A/g in a potential window of 1.7 V to evaluate the $C2F_T$ SC durability test (shown in Figure 10b). Capacitance retention remains above 96% after 800 cycles, indicating that the supercapacitor exhibits remarkable electrochemical stability. To demonstrate the high performance of $C2F_T$ SC, the charged device was used to rotate an armature, demonstrating the practical application of $C2F_T$ SC (see the Supporting Movie).

4. CONCLUSIONS

In this research, an iron nanoparticle wrapped with N-doped carbon material (C2F) was synthesized using a ZHF nanohybrid precursor. The carbon material contained amorphous and graphitic regions where iron nanoparticles showed a single-crystal structure (cubic α phase). The obtained C2F carbon material was used as an active material in the manufacture of supercapacitor electrodes. We used different conventional aqueous (sodium sulfate) and organic ($TEABF_4$ in acetonitrile) electrolytes and introduced a new electrolyte (KCN in methanol). The best results were obtained for SCs fabricated using organic $TEABF_4$ electrolyte as well as the new KCN electrolyte. So, the capacitance value was about 21 and 23 F/g at the charge−discharge current density of 0.1 A/g for $C2F_T$ and $C2F_K$ SC devices. The $C2F_T$ SC showed a maximum energy density value of 11.43 Wh/kg at a power density of 400 W/kg among all SCs. This SC showed excellent electrochemical stability due to retaining 96% of the capacitance after 800 charge−discharge cycles. These C_s values for the fabricated SCs are comparable to those of the highest-performing commercial SC devices.

■ ASSOCIATED CONTENT

Supporting Information

The Supporting Information is available free of charge at https://pubs.acs.org/doi/10.1021/acsomega.3c02017.

https://doi.org/10.1021/acsomega.3c02017
ACS Omega 2023, 8, 22964−22974

Physical and electrochemical data of the precursor and produced carbon materials (PDF)

Video of SC performance (MP4)

AUTHOR INFORMATION

Corresponding Author

Mohammad Yeganeh Ghotbi − *Materials Engineering Department, Faculty of Engineering, Malayer University, Malayer 65741-84621, Iran;* orcid.org/0000-0002-4828-3236; Phone: + 98-8133339841; Email: m.yeganeh@malayeru.ac.ir, yeganehghotbi@gmail.com

Authors

Madineh Farhadi − *Materials Engineering Department, Faculty of Engineering, Malayer University, Malayer 65741-84621, Iran*

Fatemeh Abbasi − *Materials Engineering Department, Faculty of Engineering, Malayer University, Malayer 65741-84621, Iran*

Complete contact information is available at: https://pubs.acs.org/10.1021/acsomega.3c02017

Author Contributions

M.Y.G.: supervision, conceptualization, project administration, writing—review and editing, and validation. M.F. and F.A.: material synthesis, formal analysis, and investigation.

Notes

The authors declare no competing financial interest.

ACKNOWLEDGMENTS

The authors would like to thank Malayer University (Grant No. 84.5-251) for supporting this work.

REFERENCES

(1) Chen, X.; Paul, R.; Dai, L. Carbon-Based Supercapacitors for Efficient Energy Storage. *Natl. Sci. Rev.* **2017**, *4*, 453−489.

(2) Yeganeh Ghotbi, M.; Javanmard, A.; Soleimani, H. Layered Nanoreactor Assisted to Produce B-Doped and P-Doped 3D Carbon Nanostructures for Supercapacitor Electrodes. *J. Energy Storage* **2021**, *44*, No. 103514.

(3) Yeganeh Ghotbi, M.; Azadfalah, M. Design of a Layered Nanoreactor to Produce Nitrogen Doped Carbon Nanosheets as Highly Efficient Material for Supercapacitors. *Mater. Des.* **2016**, *89*, 708−714.

(4) Jin, X.; Wang, X.; Liu, Y.; Kim, M.; Cao, M.; Xie, H.; Liu, S.; Wang, X.; Huang, W.; Nanjundan, A. K.; et al. Nitrogen and Sulfur Co-Doped Hierarchically Porous Carbon Nanotubes for Fast Potassium Ion Storage. *Small* **2022**, *18*, No. 2203545.

(5) Yeganeh Ghotbi, M.; Javanmard, A.; Soleimani, H. Three Dimensional Metal/N-Doped Nanoplate Carbon Catalysts for Oxygen Reduction, the Reason for Using a Layered Nanoreactor. *Sci. Rep.* **2018**, *8*, No. 3404.

(6) Kim, M.; Firestein, K. L.; Fernando, J. F. S.; Xu, X.; Lim, H.; Golberg, D. V.; Na, J.; Kim, J.; Nara, H.; Tang, J.; Yamauchi, Y. Strategic Design of Fe and N Co-Doped Hierarchically Porous Carbon as Superior ORR Catalyst: From the Perspective of Nanoarchitectonics. *Chem. Sci.* **2022**, *13*, 10836−10845.

(7) Zhu, S.; Wang, L.; Gu, C.; Liu, H.; Mu, Y.; Ni, J.; Han, G. Boosting Capacitive Performance of Nitrogen-Doped Carbon by Atomically Dispersed Iron. *J. Power Sources* **2022**, *532*, No. 231335.

(8) Yang, Y.; Shao, Z.; Wang, F. Preparation of Fe/N Co-Doped Hierarchical Porous Carbon Nanosheets Derived From Chitosan Nanofibers for High-Performance Supercapacitors. *J. Electrochem. Energy Convers. Storage* **2022**, *19*, No. 021009.

(9) Kim, M.; Wang, C.; Earnshaw, J.; Park, T.; Amirilian, N.; Ashok, A.; Na, J.; Han, M.; Rowan, A. E.; Li, J.; et al. Co, Fe and N Co-Doped 1D Assembly of Hollow Carbon Nanoboxes for High-Performance Supercapacitors. *J. Mater. Chem. A* **2022**, *10*, 24056−24063.

(10) Yeganeh Ghotbi, M.; Feli, B.; Azadfalah, M.; Javaheri, M. Ultra High Performance N-Doped Carbon Catalysts for the ORR Derived from the Reaction between Organic-Nitrate Anions inside a Layered Nanoreactor. *RSC Adv.* **2015**, *5*, 92577−92584.

(11) Yeganeh Ghotbi, M.; Abbasi, F. Effect of the Second Heat Treatment on the Porosity and Conductivity of a Template-Synthesized Carbon Material for Use in Supercapacitor Electrodes. *Solid State Sci.* **2022**, *128*, No. 106871.

(12) Yeganeh Ghotbi, M. Solid State Electrolytes for Electrochemical Energy Devices. *J. Mater. Sci. Mater. Electron.* **2019**, *30*, 13835−13854.

(13) Hussein, M. Z. B.; Yeganeh Ghotbi, M. Y.; Yahaya, A. H.; Abd Rahman, M. Z. The Effect of Polymers onto the Size of Zinc Layered Hydroxide Salt and Its Calcined Product. *Solid State Sci.* **2009**, *11*, 368−375.

(14) Silva, M. N. T.; Ardisson, J.; Fabri, J.; Nossol, E. Zinc Hexacyanoferrate/Multi-Walled Carbon Nanotubes Films for Rechargeable Aqueous Batteries. *J. Braz. Chem. Soc.* **2020**, *31*, 1787−1795.

(15) Jassal, V.; Shanker, U.; Kaith, B. S.; Shankar, S. Green Synthesis of Potassium Zinc Hexacyanoferrate Nanocubes and Its Potential Application in Photocatalytic Degradation of Organic Dyes. *RSC Adv.* **2015**, *5*, 26141−26149.

(16) Bagkar, N.; Ganguly, R.; Choudhury, S.; Hassan, P. A.; Sawant, S.; Yakhmi, J. V. Synthesis of Surfactant Encapsulated Nickel Hexacyanoferrate Nanoparticles and Deposition of Their Langmuir−Blodgett Film. *J. Mater. Chem.* **2004**, *14*, 1430−1436.

(17) Pang, H.; Zhang, Y.; Cheng, T.; Lai, W.-Y.; Huang, W. Uniform Manganese Hexacyanoferrate Hydrate Nanocubes Featuring Superior Performance for Low-Cost Supercapacitors and Nonenzymatic Electrochemical Sensors. *Nanoscale* **2015**, *7*, 16012−16019.

(18) Rather, M. S.; Majid, K.; Wanchoo, R. K.; Singla, M. L. Synthesis, Characterization, and Thermal Study of Polyaniline Composite with the Photoadduct of Potassium Hexacyanoferrate (II) Involving Hexamine Ligand. *J. Therm. Anal. Calorim.* **2013**, *112*, 893−900.

(19) Xu, Y.; Chang, M.; Fang, C.; Liu, Y.; Qiu, Y.; Ou, M.; Peng, J.; Wei, P.; Deng, Z.; Sun, S.; et al. In Situ FTIR-Assisted Synthesis of Nickel Hexacyanoferrate Cathodes for Long-Life Sodium-Ion Batteries. *ACS Appl. Mater. Interfaces* **2019**, *11*, 29985−29992.

(20) Thommes, M.; Kaneko, K.; Neimark, A. V.; Olivier, J. P.; Rodriguez-reinoso, F.; Rouquerol, J.; Sing, K. S. W. Physisorption of Gases, with Special Reference to the Evaluation of Surface Area and Pore Size Distribution. *Pure Appl. Chem.* **2015**, *87*, 1051−1069.

(21) Sing, K. S. W.; Everet, D. H.; Haul, R. A. W. Provisional International Union of Pure and Applied Chemistry Commission on Colloid and Surface Chemistry Subcommittee on Reporting Gas Adsorption Data. *Pure Appl. Chem.* **1985**, *57*, 603−619.

(22) Merlet, C.; Pean, C.; Rotenberg, B.; Madden, P. A.; Daffos, B.; Taberna, P.; Simon, P.; Salanne, M. Highly Confined Ions Store Charge More Efficiently in Supercapacitors. *Nat. Commun.* **2013**, *4*, No. 2701.

(23) Klinger, M. More Features, More Tools, More CrysTBox. *J. Appl. Crystallogr.* **2017**, *50*, 1226−1234.

(24) Tian, K.; Wang, J.; Cao, L.; Yang, W.; Guo, W.; Liu, S.; Li, W.; Wang, F.; Li, X.; Xu, Z.; et al. Single-Site Pyrrolic-Nitrogen-Doped Sp^2-Hybridized Carbon Materials and Their Pseudocapacitance. *Nat. Commun.* **2020**, *11*, No. 3884.

(25) Zhao, M.; Cao, Y.; Liu, X.; Deng, J.; Li, D.; Gu, H. Effect of Nitrogen Atomic Percentage on N^+-Bombarded MWCNTs in Cytocompatibility and Hemocompatibility. *Nanoscale Res. Lett.* **2014**, *9*, 142.

(26) Banda, H.; Daffos, B.; Périé, S.; Chenavier, Y.; Dubois, L.; Aradilla, D.; Pouget, S.; Simon, P.; Crosnier, O.; Taberna, P.; et al.

Ion Sieving Effects in Chemically Tuned Pillared Graphene Materials for Electrochemical Capacitors Ion Sieving Effects in Chemically Tuned Pillared Graphene Materials for Electrochemical Capacitors. *Chem. Mater.* **2018**, *30*, 3040−3047.
(27) Khattak, A. M.; Yin, H.; Ghazi, Z. A.; Liang, B.; Iqbal, A.; Khan, N. A.; Gao, Y.; Li, L.; Tang, Z. Three Dimensional Iron Oxide/Graphene Aerogel Hybrids as All-Solid-State Flexible Supercapacitor Electrodes. *RSC Adv.* **2016**, *6*, 58994−59000.
(28) Anantharaj, S.; Noda, S. IR Drop Correction in Electrocatalysis: Everything One Needs to Know! *J. Mater. Chem. A* **2022**, *10*, 9348−9354.
(29) Wang, X.; Zhang, Y.; Zhi, C.; Wang, X.; Tang, D.; Xu, Y.; Weng, Q.; Jiang, X.; Mitome, M.; Golberg, D.; Bando, Y. Three-Dimensional Strutted Graphene Grown by Substrate-Free Sugar Blowing for High-Power-Density Supercapacitors. *Nat. Commun.* **2013**, *4*, No. 2905.
(30) Bora, C.; Sharma, J.; Dolui, S. Polypyrrole/Sulfonated Graphene Composite as Electrode Material for Supercapacitor. *J. Phys. Chem. C* **2014**, *118*, 29688−29694.
(31) Yadlapalli, R. T.; Alla, R. R.; Kandipati, R.; Kotapati, A. Super Capacitors for Energy Storage: Progress, Applications and Challenges. *J. Energy Storage* **2022**, *49*, No. 104194.
(32) Kumar, N.; Kim, S.-B.; Lee, S.-Y.; Park, S.-J. Recent Advanced Supercapacitor: A Review of Storage Mechanisms, Electrode Materials, Modification, and Perspectives. *Nanomaterials* **2022**, *12*, 3708.

https://doi.org/10.1021/acsomega.3c02017
ACS Omega 2023, 8, 22964−22974